11-13-2019

Fabricating Fe nanocrystals via encapsulation at the graphite surface

Ana Lii-Rosales
Iowa State University and Ames Laboratory

Yong Han
Iowa State University, y27h@iastate.edu

King C. Lai
Iowa State University and Ames Laboratory, kclai@iastate.edu

Dapeng Jing
Iowa State University

Michael C. Tringides
Iowa State University and Ames Laboratory, mctringi@ameslab.gov

See next page for additional authors

Fabricating Fe nanocrystals via encapsulation at the graphite surface

Abstract

In this paper, the authors describe the conditions under which Fe forms encapsulated nanocrystals beneath the surface of graphite, and they characterize these islands (graphite + Fe) thoroughly. The authors use the experimental techniques of scanning tunneling microscopy (STM) plus x-ray photoelectron spectroscopy (XPS) and the computational technique of density functional theory (DFT). Necessary conditions for encapsulation are preexisting ion-induced defects in the graphite substrate and elevated deposition temperature of 875–900 K. Evidence of encapsulation consists of atomically resolved STM images of a carbon lattice, both on top of the islands and on the sloping sides. The nature of the images indicates that this carbon lattice corresponds to a graphene blanket consisting of more than one graphene sheet that drapes continuously from the top of the island to the graphite substrate. The formation of iron carbide is not observed based on XPS. Shapes of the island footprints are consistent with metallic Fe, predominantly in the hcp or fcc form, though larger islands tend toward bcc. Island structures with hexagonally close-packed lateral hcp or fcc planes are stabilized by their excellent lattice match with the graphite substrate. Evolution of island density with prolonged deposition time provides evidence of coarsening, perhaps via Smoluchowski ripening. The encapsulated Fe clusters are stable in air at room temperature, protected by smaller Fe clusters that decorate defect sites and block permeation of gases. DFT shows that two configurations of Fe are more stable within the gallery than adsorbed on top of the surface: a single atom of Fe and a film (slab) of metallic Fe. Comparison with other metals shows that encapsulated Fe is similar to Cu but dissimilar to Ru or Dy, leading the authors to conclude that carbon dissolution in the metal does not play a role in encapsulation.

Keywords

Graphene, Iron, Density functional theory, X-ray photoelectron spectroscopy, Thin films, Carbon based materials, Nanocrystals, Scanning tunneling microscopy

Disciplines

Chemistry | Materials Science and Engineering | Nanoscience and Nanotechnology | Physics

Authors

Ana Lii-Rosales, Yong Han, King C. Lai, Dapeng Jing, Michael C. Tringides, James W. Evans, and Patricia A. Thiel

Fabricating Fe nanocrystals via encapsulation at the graphite surface

Ann Lii-Rosales, Yong Han, King C. Lai, Dapeng Jing, Michael C. Tringides, James W. Evans, and Patricia A. Thiel

Citation: Journal of Vacuum Science & Technology A **37**, 061403 (2019); doi: 10.1116/1.5124927
View online: https://doi.org/10.1116/1.5124927
View Table of Contents: https://avs.scitation.org/toc/jva/37/6
Published by the American Vacuum Society

Fabricating Fe nanocrystals via encapsulation at the graphite surface

Ann Lii-Rosales,[1,2,a)] Yong Han,[1,3] King C. Lai,[1,3] Dapeng Jing,[4] Michael C. Tringides,[1,3] James W. Evans,[1,3] and Patricia A. Thiel[1,2,5,b)]
[1]*Ames Laboratory, Ames, Iowa 50011*
[2]*Department of Chemistry, Iowa State University, Ames, Iowa 50011*
[3]*Department of Physics and Astronomy, Iowa State University, Ames, Iowa 50011*
[4]*Materials Analysis and Research Laboratory, Iowa State University, Ames, Iowa 50011*
[5]*Department of Materials Science and Engineering, Iowa State University, Ames, Iowa 50011*

(Received 18 August 2019; accepted 11 October 2019; published 13 November 2019)

In this paper, the authors describe the conditions under which Fe forms encapsulated nanocrystals beneath the surface of graphite, and they characterize these islands (graphite + Fe) thoroughly. The authors use the experimental techniques of scanning tunneling microscopy (STM) plus x-ray photoelectron spectroscopy (XPS) and the computational technique of density functional theory (DFT). Necessary conditions for encapsulation are preexisting ion-induced defects in the graphite substrate and elevated deposition temperature of 875–900 K. Evidence of encapsulation consists of atomically resolved STM images of a carbon lattice, both on top of the islands and on the sloping sides. The nature of the images indicates that this carbon lattice corresponds to a graphene blanket consisting of more than one graphene sheet that drapes continuously from the top of the island to the graphite substrate. The formation of iron carbide is not observed based on XPS. Shapes of the island footprints are consistent with metallic Fe, predominantly in the hcp or fcc form, though larger islands tend toward bcc. Island structures with hexagonally close-packed lateral hcp or fcc planes are stabilized by their excellent lattice match with the graphite substrate. Evolution of island density with prolonged deposition time provides evidence of coarsening, perhaps via Smoluchowski ripening. The encapsulated Fe clusters are stable in air at room temperature, protected by smaller Fe clusters that decorate defect sites and block permeation of gases. DFT shows that two configurations of Fe are more stable within the gallery than adsorbed on top of the surface: a single atom of Fe and a film (slab) of metallic Fe. Comparison with other metals shows that encapsulated Fe is similar to Cu but dissimilar to Ru or Dy, leading the authors to conclude that carbon dissolution in the metal does not play a role in encapsulation. *Published by the AVS.*
https://doi.org/10.1116/1.5124927

I. INTRODUCTION

The ability to embed metallic structures in layered materials holds promise for applications in microelectronics or nanoelectronics, where the metals may be useful as electrical contacts or heat sinks in circuits that involve two-dimensional materials. The embedded metallic nanoparticles may also be useful as catalysts or magnets, especially in cases where the two-dimensional blanket protects the metal from oxidation or inhibits sintering. We have recently demonstrated that a variety of metals—Cu, Ru, Dy—can be grown as metallic particles embedded beneath the surface of graphite, provided growth conditions are chosen appropriately.[1–3]

In the present paper, we show that Fe can also undergo encapsulation, and we characterize the Fe islands thoroughly. The main goal is to compare the behavior of Fe with that of the other metals.[1–3] On the one hand, similarities might be expected between Fe and Cu since the two transition metals are adjacent in the Periodic Table. On the other hand, Cu is generally less reactive than Fe, Dy, or Ru. In particular, Fe, Dy, and Ru are known to have much higher affinities for carbon than does Cu. For instance, the maximum solubility of C in solid Fe is 2.4% by weight (achieved in fcc Fe at 1420 K),[4] and in Cu it is 0.0076% (achieved at 1360 K).[5] Furthermore, Fe (and also Dy and Ru) forms thermodynamically stable carbides, whereas Cu does not.[4,6–9]

We thus expect that a comparison of these metals will reveal whether carbon dissolution in the metal, or metal carbide formation, is a defining feature with respect to encapsulation.

It is relevant to briefly review the body of work dealing with graphene growth on Fe and Cu surfaces. Carbide formation is ubiquitous for Fe,[10] and special procedures are necessary to circumvent this problem. For example, graphene can be grown on Fe(110) in ultrahigh vacuum (UHV) via chemical vapor deposition (CVD).[11] Carbide formation can be avoided by using highly nonequilibrium growth conditions where excess C ($\sim 10^{-7}$ mbar of a hydrocarbon precursor) suppresses Fe carbide formation and favors graphene growth. Graphene can also be grown on Fe via CVD in a high pressure (10 Torr) environment.[12] Here, growth involves carburization processes where C is dissolved into bulk Fe at growth temperatures and segregates to the surface upon cooling.[12]

Note: This paper is part of the Special Topic Collection on 30 years of the Nellie Yeoh Whetten Award — Celebrating the Women of the AVS.
[a)]Present address: Department of Chemistry, University of Colorado Boulder, Boulder, Colorado 80309; electronic mail: ann.lii-rosales@colorado.edu
[b)]Electronic mail: pthiel@ameslab.gov

This results in graphene that coexists with metallic Fe and Fe carbide. In CVD growth of graphene on Cu, on the other hand, it is generally believed that dissolution of C in the bulk is negligible and precipitation upon cooling from growth temperatures does not play a role.[13–18]

Nanoscale Fe is, of course, interesting in its own right. Bulk Fe (bcc structure) is ferromagnetic. However, low-dimensional Fe, for example thin films and nanostructures, has various magnetic properties that are highly sensitive to electron hybridization and structural dynamics.[19] Fe is also an excellent catalyst in Fischer–Tropsch reactions and in ammonia synthesis.[20,21] Fe nanoparticles are also effective agents for environmental remediation.[22]

This paper is organized as follows. Experimental and computational methods are described briefly in Sec. II. Experimental results are presented in Sec. III and computational results in Sec. IV. Discussion and concluding remarks comprise Secs. V and VI, respectively. Further details relevant to Secs. II–IV are available in the supplementary material.[67]

II. EXPERIMENTAL AND COMPUTATONAL METHODS

A. Experimental methods

All experiments were performed in an Omicron UHV chamber with base pressure in the low 10^{-11} mbar range. Briefly, Fe was deposited via physical vapor deposition from an *e*-beam evaporator, where metallic Fe was contained in a W crucible lined with Al_2O_3. The Fe flux was about 0.2 monolayer per minute. Commercial highly oriented pyrolytic graphite (HOPG, ZYA grade) was the substrate for all depositions. Two types of graphite substrates were prepared: a pristine surface (referred to as p-graphite hereafter) via *ex situ* Scotch tape exfoliation and an ion-bombarded surface (i-graphite) prepared by transfer into UHV and Ar ion bombardment after exfoliation. Experimental observation and characterization of the i-graphite surface are reported in previous work by our group and others.[1,23,24] Fe was deposited onto either type of graphite surface while the graphite sample was held at different temperatures, T_{dep}. The Fe/graphite samples were carefully characterized by scanning tunneling microscopy (STM) and x-ray photoelectron spectroscopy (XPS), both performed at room temperature in UHV. Additional experimental details are given in the supplementary material.[67]

B. Computational techniques: DFT method and benchmarking

We performed first-principles DFT total-energy calculations for the Fe-graphene and Fe-graphite systems using the Vienna *Ab Initio* Simulation Package (VASP) code.[25] The projector-augmented-wave method[26] was used for the electron-core interactions. The pseudopotentials were generated and released in 2013 by the VASP group. For all Fe-C systems, we used the optB88-vdW functional, where the exchange functional is optimized for the correlation part,[27] to approximately account for dispersion interactions. The Γ-centered $\boldsymbol{k}$ mesh will be specified for each system. The force-convergence criterion was 0.1 eV/nm. For surface systems, the vacuum thickness between two adjacent slab replicas was not less than 1.5 nm. Spin-polarization effects and dipole corrections have been taken into account unless noted otherwise.

From our previous DFT calculations,[28] the optB88-vdW functional can reproduce very well the experimental lattice constants, cohesive energy, and exfoliation energy of graphite (the AB-stacked hexagonal structure[29]), as well as experimental lattice constant of a graphene monolayer (GML). We also already used the optB88-vdW functional to analyze the Cu-C (Refs. 1, 28, and 30) and Ru-C (Ref. 2) systems, obtaining desired energetics. Here, we make benchmark calculations for the bulk properties (lattice constants and cohesive energies) of α-Fe (bcc phase), γ-Fe (fcc phase), and ε-Fe (hcp phase). From our optB88-vdW calculations, the energetically most favorable bcc, fcc, and hcp structures of Fe are ferromagnetic, antiferromagnetic, and nonmagnetic, respectively. This result is consistent with Herper *et al.*'s DFT calculations.[31] Table I lists the lattice constants and cohesive energies of bcc, fcc, and hcp Fe from this work using optB88-vdW and available experimental values. The cohesive energy is calculated as $E_{coh} = E_{gas} = \sigma_{bulk}$, where σ_{bulk} is the energy per atom in the unit cell, and E_{gas} is the energy of one atom in gas phase. We have also calculated some quantities using the PBE, PBE-TS and PBEsol functionals; those results are tabulated in the supplementary material.[67] In no case do they give better agreement with experiment than optB88-vdW. The ability of the optB88-vdW functional to describe Fe well, and also graphite and graphene, justifies its choice for all Fe-C systems in this work. However, it is worth noting that an unusually large number of relaxation steps for the electronic degrees of freedom, and all-band simultaneous update of orbitals, are needed during the structure optimization in order to obtain the

TABLE I. Lattice constants (*a* and *c*, or *a*) and cohesive energies (E_{coh}) of bcc, fcc, and hcp Fe from our DFT calculations vs previous experiments. The $\boldsymbol{k}$ meshes and cutoff energies (E_{cut}) used in our DFT calculations are also listed.

System	Method	E_{cut} (eV)	$\boldsymbol{k}$ mesh	*a* (nm)	*c* (nm)	E_{coh} (eV)
α-Fe (bcc)	optB88-vdW	400	61 × 61 × 61	0.2822		5.049
	optB88-vdW	600	61 × 61 × 61	0.2823		5.049
	Experiment			0.2866[a]		4.28[b]
γ-Fe (fcc)	optB88-vdW	600	61 × 61 × 61	0.3470		4.977
	Experiment			0.35692[c]		
ε-Fe (hcp)	optB88-vdW	600	61 × 61 × 61	0.2459	0.3879	5.038
	Experiment			0.2524[d]	0.4046[d]	

[a]At room temperature (Ref. 32).
[b]Reference 33.
[c]Extrapolated from the data of Fe-C and Fe-N alloys at room temperature (Ref. 34).
[d]Extrapolated from the high-pressure data at 23 ± 3 °C using the Murnaghan equation of state (Ref. 35).

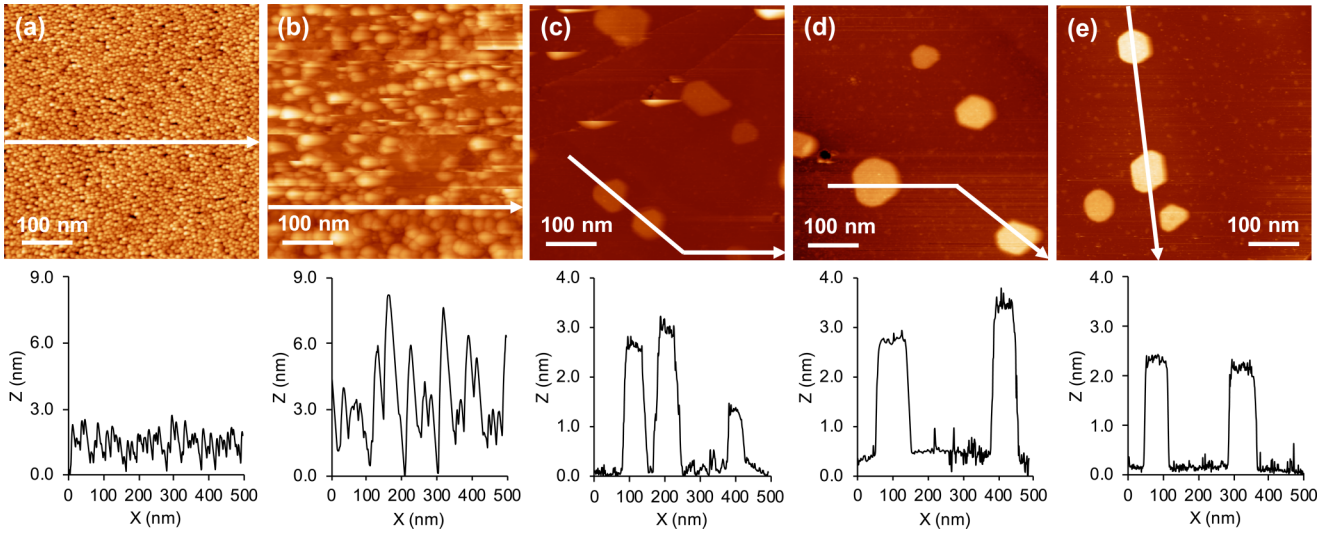

FIG. 1. Representative topographic STM images and line profiles after five separate depositions of Fe on i-graphite. (a) 300 K, (b) 800 K, (c) 875 K, (d) 888 K, and (e) 900 K. Time of deposition in each experiment is (a) and (e) 45 min and (b)–(d) 90 min. Tip bias and tunneling current are (a) +2.0 V, 0.26 nA; (b) +4.5 V, 0.25 nA; (c) +3.9 V, 0.26 nA; (d) +4.5 V, 0.26 nA; and (e) +4.4 V, 0.27 nA.

minimized energy of a mixed Fe-C system using the optB88-vdW functional.

III. EXPERIMENTAL RESULTS

A. Conditions necessary to form encapsulated islands and island dimensions

The morphology of Fe grown on i-graphite depends strongly on T_{dep}, as shown in Fig. 1. At 300 K, Fe forms small and round clusters that are 2–3 nm tall on top of graphite. At a higher $T_{dep} = 800$ K, Fe agglomerates into larger and taller clusters compared to those formed at 300 K. The clusters are bare Fe, as evident from their streakiness in imaging [Fig. 1(b)], which is caused by the STM tip picking up or removing clusters. Dramatic morphology changes occur starting at 875 K. First, the graphite terraces become much cleaner. Some tall, bare clusters persist, but they become very rare at 900 K. They are still distinguished by their streakiness, as evident in Fig. 1(c). Second, new features develop—islands of a few nanometers in height, with flat tops and well-defined footprints that are usually faceted. Unlike the bare Fe clusters, these features are very stable under tunneling conditions. Additional examples are shown in Fig. 2. In Sec. III B, we present evidence that these stable flat-top features are Fe clusters covered by a graphene blanket. (The blanket and metal cluster together is termed an island.)

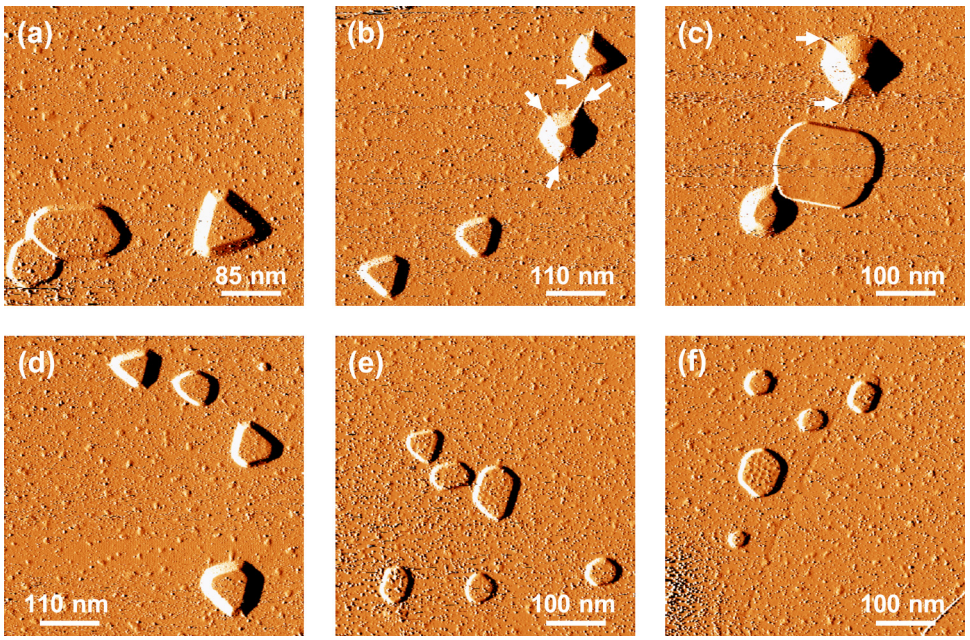

FIG. 2. Additional STM images of encapsulated Fe clusters deposited at (a)–(d) 900 K for 180 min and (e)–(f) 900 K for 45 min. White arrows in (b) and (c) point to wrinkles in the graphene overlayer. All STM images are derivatized. Tip bias and tunneling current are (a) +3.0 V, 0.26 nA; (b) +2.6 V, 0.26 nA; (c) +2.5 V, 0.26 nA; (d) +2.9 V, 0.26 nA; (e) +3.7 V, 0.26 nA; and (f) +3.5 V, 0.26 nA.

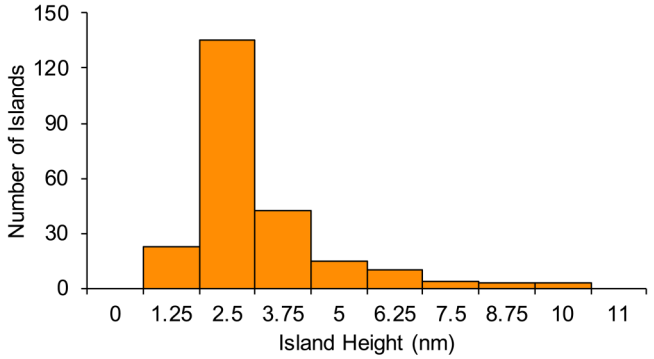

FIG. 3. Height histogram of encapsulated Fe islands observed at $T_{dep} = 875$–950 K. 235 islands are included, with an average height of 2.5 ± 1.6 nm. Bin size is 1.25 nm.

The mean measured height is 2.5 ± 1.6 nm for all flat-topped islands observed. A height histogram of the islands is shown in Fig. 3. Based on DFT results to be presented in Sec. IV B, the average height of 2.5 nm corresponds to about 13 Fe monolayers, with the full range spanning 6–60 Fe monolayers. The average width of the flat top is about 50 nm, i.e., about 20 times the average height. Note that in all STM profiles presented in this paper, such as Fig. 1, the x- and y-axes are drawn to different scales in order to produce compact figures. If the axes were drawn with equal scales, it would be apparent that the widths of the flat-topped islands are much greater than their heights. Dimensions of the flat-topped islands are evaluated extensively elsewhere.[36]

The combination of elevated T_{dep} and preexisting defects from ion bombardment are essential conditions for encapsulation. This is demonstrated by control experiments in which each condition is selectively removed. Figure 4 shows the first control experiment, in which Fe is deposited on i-graphite without elevated T_{dep} but with induced defects. Bare Fe clusters are observed upon deposition at 300 K [Figs. 4(a)–4(c)], and they simply coarsen after annealing at 900 K [Figs. 4(d)–4(f)], as evidenced by increases in cluster height and area. Figure 5 shows the

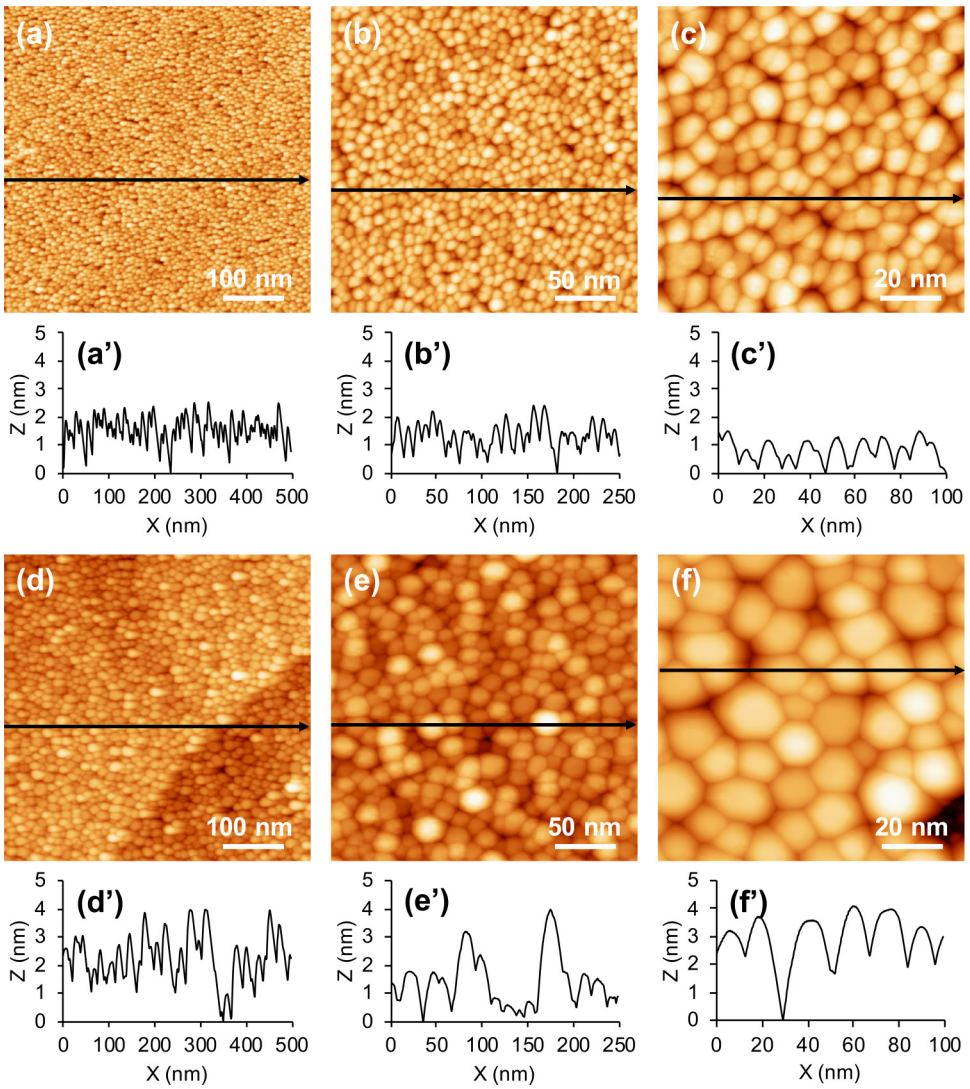

FIG. 4. Control experiment with Fe [(a)–(c)] deposited on i-graphite at 300 K for 45 min followed by [(d)–(f)] annealing at 900 K for 45 min. All STM images are topographic. Corresponding line profiles are shown in (a′)–(f′). Tip bias and tunneling current are (a)–(c) +2.0 V, 0.26 nA; (d) +3.0 V, 0.26 nA; (e) −2.6 V, 0.26 nA; and (f) +2.6 V, 0.26 nA.

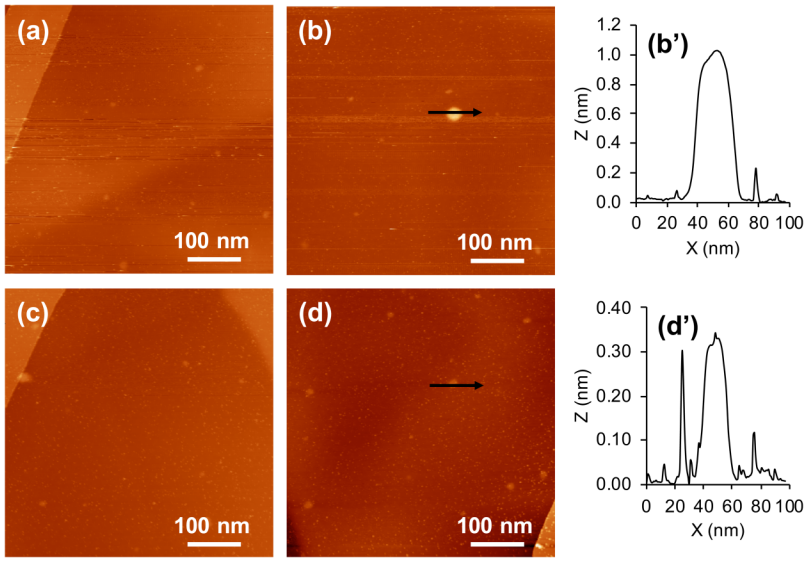

FIG. 5. Control experiment of Fe deposited on p-graphite at 900 K for 45 min. All STM images are topographic. Tip bias and tunneling current are (a) and (b) +1.7 V, 0.26 nA; (c) +1.2 V, 0.26 nA; and (d) +1.5 V, 0.26 nA.

second control experiment, with elevated T_{dep} but without induced defects. After deposition on p-graphite at 900 K, the graphite surfaces remain relatively clean and free of Fe decoration. Rarely, we observe a few protruding features, but their overall dimensions and appearance are not comparable to those of the Fe islands seen in Figs. 1(c)–1(e). Thus, these control experiments clearly demonstrate that both conditions are necessary to form encapsulated Fe clusters.

In addition to large bare Fe clusters and encapsulated Fe clusters, smaller features are evident on the surface at high magnification, as shown in Fig. 6. Most of these have a discrete, lumpy shape. We interpret them as bare Fe clusters consisting of one or a few Fe atoms anchored at defects. However, not all graphite defects are decorated by Fe atoms. For example, the defect in the top left corner of Fig. 6(a) has a diffuse threefold star shape that is the signature of a single-carbon-atom vacancy in graphite.[37] A similar defect is evident in Fig. 7(b″).

B. STM evidence of encapsulation by graphene multilayers

To further characterize the flat Fe islands that form at 875–900 K, we obtain atomically resolved images of the island tops and sloping sides. At high resolution, the tops of islands [Figs. 7(a″)–7(d″)] usually show triangular arrays of C atoms with a measured spacing of 0.247 ± 0.003 nm (from 30 measurements). This spacing agrees well with the graphite lattice constant of 0.246 nm.[38] Furthermore, the C lattice is continuous from the island top onto the graphite substrate, as shown in Fig. 7(a″). This is firm evidence of encapsulation of Fe at the graphite surface.

Notably, some Fe islands exhibit sharp, pointed features that radiate from the edge of the island. Examples are indicated by white arrows in Figs. 2(b) and 2(c). We attribute these to wrinkles that form in the graphene blanket during its delamination from the graphite substrate.[39] These are further evidence of encapsulation of the metal. Also, they serve as evidence that the space beneath the sloping side is empty, since any underlying material would interfere with folding.[39] Our proposal for the structure of the encapsulated cluster is depicted schematically in Fig. 8.

The detailed appearance of the C lattice in STM sheds further insight. A honeycomb lattice, in which all six C atoms in each ring are imaged equivalently, can signal several configurations: (1) a single freestanding graphene sheet; (2) multiple graphene sheets stacked such that the sixfold symmetry of the topmost sheet is unperturbed, i.e., A-A stacking; or (3) a graphene bilayer in which the bottom

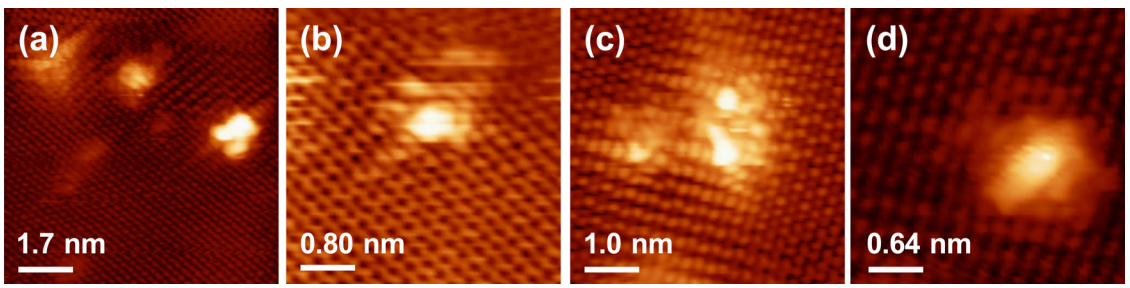

FIG. 6. STM images of defect-related features at high magnification. Images (a) and (b) are from the tops of encapsulated Fe islands and (c) and (d) are from the graphite substrate, following Fe deposition at 900 K. Tip bias and tunneling current are (a) and (b) +0.08 V, 0.39 nA and (c) and (d) +0.07 V, 0.39 nA.

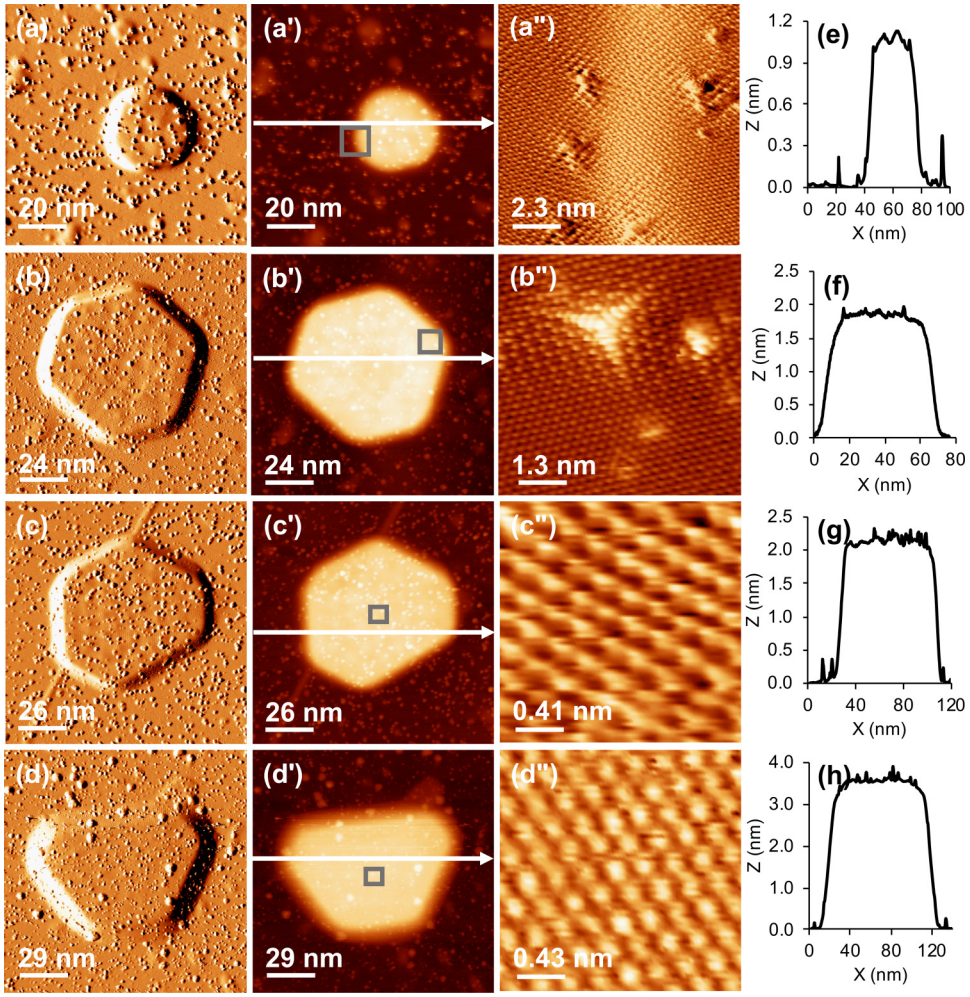

FIG. 7. Representative high-resolution STM images of encapsulated Fe clusters formed at 900 K from four separate experiments with various deposition time: (a)–(d) 22.5, 45, 90, and 90 min, respectively. (a)–(d) are derivative images and (a′)–(d′) are topographic images. (a″) is a derivative image that shows continuous C lattice over island slope, while (b″)–(d″) are topographic images that show C lattice on island top. Tip bias and tunneling current are (a) +1.7 V, 0.26 nA; (a″) +0.15 V, 0.41 nA; (b) +1.8 V, 0.26 nA; (b″) +0.07 V, 0.39 nA; (c) +1.5 V, 0.26 nA; (c″) +0.08 V, 0.38 nA; (d) +2.2 V, 0.26 nA; and (d″) +0.09 V, 0.39 nA.

layer bonds strongly to a metal and shields the upper layer, making the upper layer appear freestanding.[40] On the other hand, a triangular lattice in which only three out of six C atoms are imaged equivalently can signal a single graphene sheet interacting strongly with a metal substrate, known to occur for Ru(0001)[40,41] and expected for Fe due to the strong metal-C interaction,[10,42] or multiple graphene sheets stacked in a way that breaks the sixfold symmetry, e.g., the conventional A-B stacking of graphite.[43]

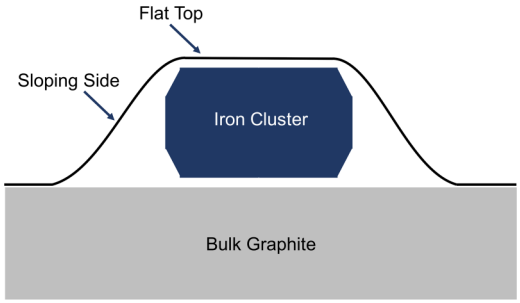

FIG. 8. Schematic cross-sectional model of an encapsulated Fe cluster.

In our experiments, the majority of graphite lattices observed on top of islands show triangular arrays where three out of six C atoms are imaged equivalently. On a few occasions (6 out of 34 islands where the lattice has been resolved), we observe a honeycomb lattice where six out of six C atoms are equivalent. These observations are open to multiple possible interpretations (above). More significant are high-resolution images on the sloping sides of seven islands. These images show triangular arrays of C atoms (three of six). Adopting the argument (above) that there is an empty gap between these sloping sides and the body of the Fe cluster, the possible explanation of strong interaction with underlying metal is eliminated. This leads to the conclusion that the sloping sides are composed of more than one GML. Because the sloping side is continuous with the top of the island, multiple GMLs must also cover the island top.

C. XPS: Evidence against carbidic Fe

Having identified the stable, flat-top islands as encapsulated Fe clusters at the graphite surface, it is important to address the chemical nature of encapsulated Fe. Fe is prone

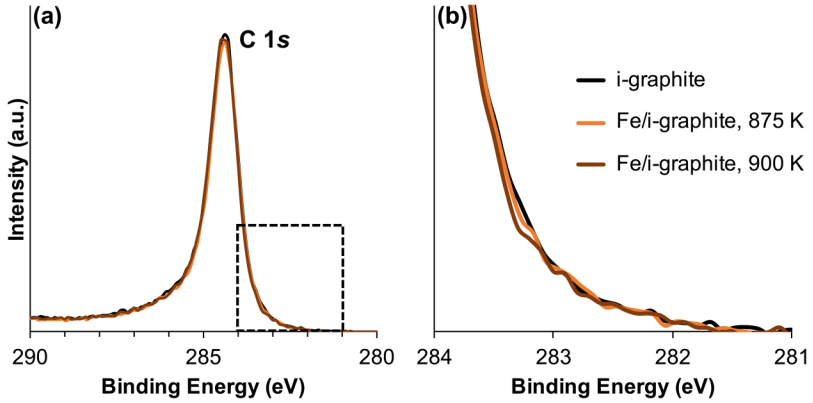

FIG. 9. Raw XP spectra comparing the C 1*s* region of plain i-graphite with that of Fe/i-graphite at 875 and 900 K where encapsulation occurs. No sign of carbide is observed around 283 eV. Boxed area in (a) is enlarged in (b). The spectra are raw, not normalized.

to form carbides, and it is present here in a C-rich environment. We use XPS to probe specifically the C 1*s* region of Fe/i-graphite (shown in Fig. 9) but not the Fe 2*p* region since it does not exhibit an appreciable chemical shift under the influence of C.[44] Studies of graphene grown on Fe show that the C 1*s* peak in Fe carbide falls in the range of 282.6–283.8 eV,[11,12,44,45] which is at significantly lower binding energy (BE) than the C 1*s* peak at 284.6 eV in graphene or graphite. In our XP spectra of the C 1*s* region, however, we do not observe a peak or shoulder around 283 eV that would indicate carbide. Therefore, we conclude that encapsulated Fe retains its metallic state without carbide formation, although it probably incorporates some dissolved carbon.

D. Island footprints: Hexagonally close-packed versus bcc Fe

Having ensured that carbide does not form, we now interpret the footprints of the encapsulated clusters in terms of metallic Fe. The majority of islands have hexagonal (or quasihexagonal) and triangular (or truncated triangular) facets. A few have round footprints, and a very few exhibit rectangular footprints. Examples of each shape are shown in Figs. 10(a)–10(h), and the shape distribution is given in Fig. 10(i). Hexagonal and triangular shapes are generally associated with hexagonal close-packed (hcp) or face-centered cubic (fcc) metallic structures. This is discussed further in the Sec. III E. The rectangular shape signals the body-centered cubic (bcc) structure in the Fe growth.[46,47] The majority of encapsulated islands are thus hcp or fcc, though bcc is the ground-state structure of bulk Fe. The fcc form has been observed previously in studies of Fe films grown on Cu(111), transforming to bcc in thicker films.[46–48] In our work, in fact, the three largest island volumes belong to rectangular islands, consistent with a structural transition from hcp or fcc to bcc for large islands. In addition, about 10% of the islands (26 out of 235) exhibit a rounded footprint. We speculate that these islands may reflect a transition from hcp or fcc to bcc. The growth of the hcp and fcc forms of Fe is probably promoted by the excellent lattice match between the hexagonally close-packed planes of the metal and the HOPG lattice, strain being less than 0.25% for both

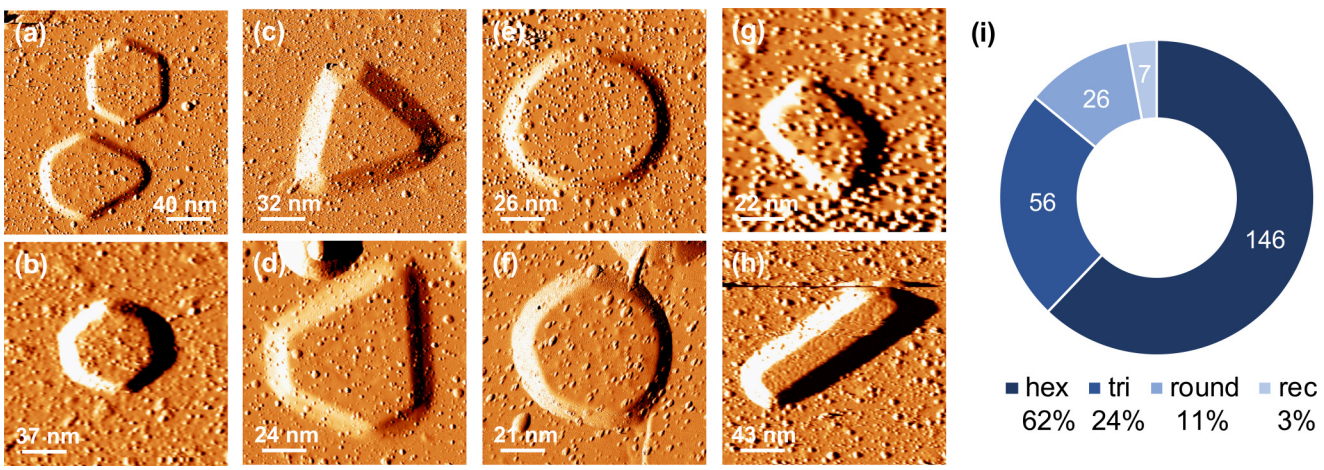

FIG. 10. Island footprints. (a) and (b) Hexagonal and quasihexagonal, (c) and (d) triangular and truncated triangular, (e) and (f) round, and (g) and (h) rectangular. All STM images are differentiated. Tip bias and tunneling current are (a) +2.6 V, 0.26 nA; (b) +4.5 V, 0.26 nA; (c) +2.0 V, 0.26 nA; (d) +3.0 V, 0.26 nA; (e) +2.0 V, 0.26 nA; (f) +1.5 V, 0.26 nA; and (g) and (h) +3.8 V, 0.26 nA. (i) Distribution of island shapes. Numbers in the ring are number of islands observed, out of a total of 235. Numbers below the ring are percentages.

hcp and fcc, from both experiment and DFT (Table I and Sec. IV B). This lattice match would, of course, be more influential for small islands than for large islands, since for large islands any deviation from the bulk structure becomes increasingly unfavorable. This is analogous to the energetic balance that leads to Stranski–Krastanov growth.[49]

E. Interpretation of facetted Fe island footprints

As indicated in Sec. III D, 62% of Fe islands display a hexagonal footprint which plausibly corresponds to the equilibrium shape. It is thus particularly appropriate to elucidate the origin of the hexagonal footprints. The DFT analysis in Sec. II B reveals an energetic preference for the bulk hcp over fcc structure (see Table I), so here we assume this is the case. An additional 24% of Fe islands display a triangular footprint, so elucidation of this feature is also appropriate.

With regard to the equilibrium shape of hcp Fe islands, it is natural to first consider the simpler situation of bare Fe clusters epitaxially supported by a hcp(0001) plane on top of graphite. Within a continuum modeling framework (which assumes linear cluster dimensions of many lattice constants), this shape is determined by a Winterbottom analysis that takes the unsupported hcp Fe Wulff shape and removes a slice adjacent to a hcp(0001) facet. This creates a somewhat larger hcp(0001) facet on which the cluster is supported. The ratio of the distance from the center of the (unsupported) cluster to the graphite substrate, h_{HOPG}, and to the top hcp(0001) facet, h_{0001}, satisfies $h_{HOPG}/h_{0001} = 1 - 2f_{HOPG}(hcp) < 1$, Here, $f_{HOPG}(hcp) = \beta_{HOPG\text{-}Fe}/(2\gamma_{0001})$, where $\beta_{HOPG\text{-}Fe}$ denotes the adhesion energy of hcp(0001) Fe to graphite and γ_{0001} denotes the surface energy of hcp(0001) Fe. DFT analysis using optB88 (cf. Sec. II B) finds that $f_{HOPG}(hcp) = 0.073$. Then, utilizing relative surface energies for the six most favorable low index surfaces of hcp Fe from PBE DFT as reported by Tran *et al.*,[50] one obtains the Winterbottom shape for hcp Fe shown in Fig. 11(a). This figure also indicates the different facets present including the top and bottom hexagonal (0001) facets and alternating vertical $(10\bar{1}0)$ and $(21\bar{3}0)$ side facets. We caution that minority facets appearing in the continuum formalism may not be present for nanoscale clusters. Of particular relevance is that lateral cross sections of this structure have sixfold symmetry about the central vertical axis, consistent with experimental observation of hexagonal island footprints [Figs. 10(a) and 10(b)].

Next, it is instructive to consider a situation closer to but still simpler than that of the experimental intercalated islands. Specifically, we consider the effect of placing a graphene sheet across the top of the above supported Fe cluster but ignore the effect of strain in that sheet. Then, the equilibrium cluster shape is determined by what we describe as a double Winterbottom construction: take the above Winterbottom shape and remove a slice adjacent to the top hcp(0001) facet, where the amount removed is controlled by a factor $f_{MLG}(hcp) = 0.067$, determined analogously to f_{HOPG}. This double Winterbottom shape for strain-free intercalation is shown in Fig. 11(b). Again, the key feature is that lateral cross sections have sixfold symmetry. The increased size of the top hexagonal facet relative to Fig. 11(a) is a consequence of removing a slice at the top of the standard Winterbottom shape. This sixfold symmetry will be preserved when the Fe cluster is compressed under intercalation, a feature compatible with the conclusion that the observed dominant population of islands with hexagonal footprints correspond to hcp structures.

Finally, we briefly describe the equilibrium shapes expected for fcc Fe islands. For bare Fe clusters epitaxially supported by

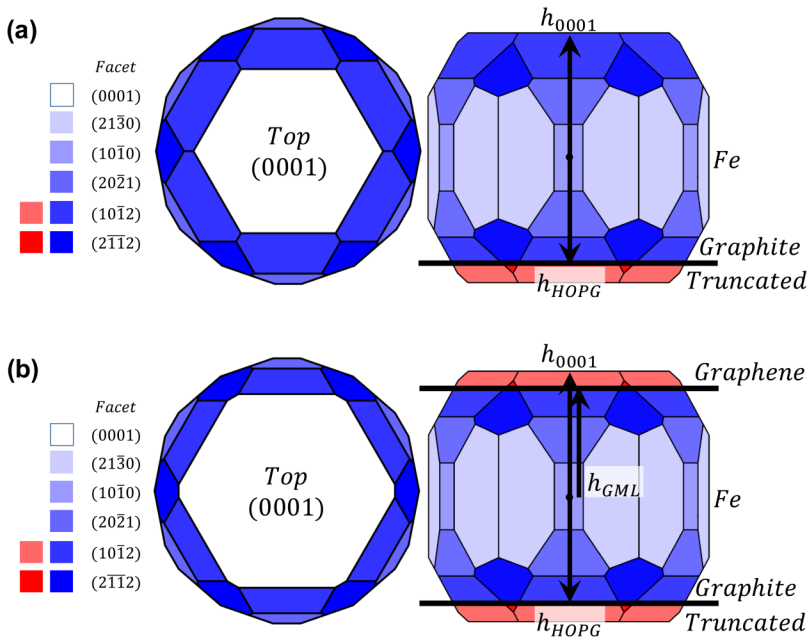

FIG. 11. Shape of an hcp Fe cluster (a) supported on top of graphite (Winterbottom) and (b) intercalated beneath the graphite surface in the absence of strain (double Winterbottom). The red colored region(s), which are above or below the thick horizontal lines, show the portion(s) of the cluster which is removed.

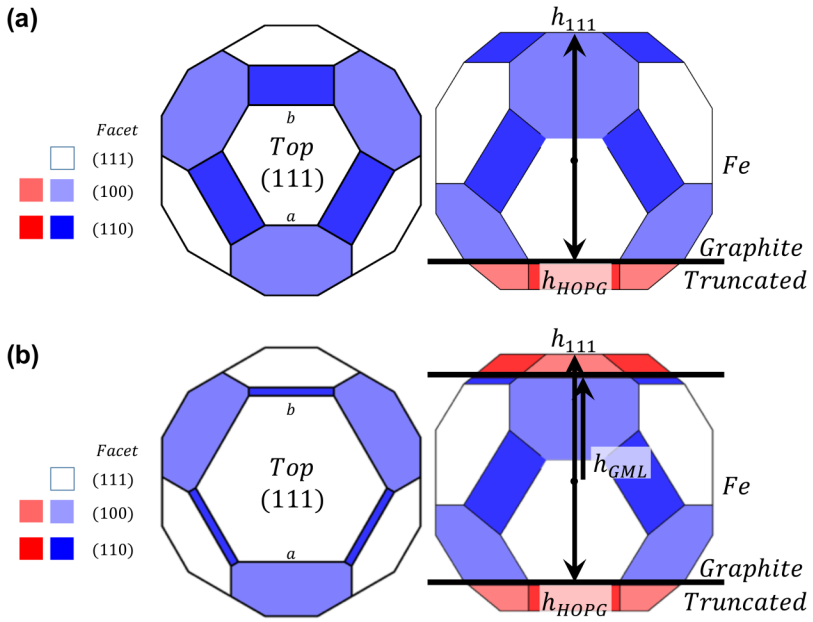

FIG. 12. Shape of an fcc Fe cluster (a) supported on top of graphite (Winterbottom) and (b) intercalated beneath the graphite surface in the absence of strain (double Winterbottom). The red colored region(s), which are above or below the thick horizontal lines, show the portion(s) of the cluster which is removed.

a fcc(111) plane on top of graphite, a Winterbottom analysis shows that $h_{HOPG}/h_{111} = 1 - 2f_{HOPG}(fcc) < 1$. Here, $f_{HOPG}(fcc) = \beta_{HOPG\text{-}Fe}/(2\gamma_{111})$, where $\beta_{HOPG\text{-}Fe}$ denotes the adhesion energy of fcc(111) Fe to graphite and γ_{111} denotes the surface energy of fcc(111) Fe. We utilize surface energies for the most favorable low index 111, 100, and 110 surfaces of fcc Fe as reported by Yu *et al.*[51] Also, we assume that $\beta_{HOPG\text{-}Fe}$ is similar for fcc(111) and hcp(0001) Fe to obtain $f_{HOPG}(fcc) = 0.102$. (Here, we note that optB88 energies are 10% higher than PBE energies so perform appropriate rescaling for consistency.) This analysis yields the Winterbottom shape for fcc Fe shown in Fig. 12(a). Similarly, we have performed a double Winterbottom construction to determine the equilibrium shape of intercalated fcc Fe clusters in the absence of strain using the value of $f_{MLG}(fcc) = 0.092$ [see Fig. 12(b)]. A key feature is that both these analyses yield top and bottom facets that are significantly distorted from hexagonal [a/b = 0.615 in Fig. 12(a) and a/b = 1.25 in Fig. 12(b)] and are quite similar to shapes observed in the experiment [Figs. 10(c) and 10(d)]. For the top facet, a/b = 0.615 for the Winterbottom construction in Fig. 12(a) and a/b = 1.25 for the double Winterbottom construction in Fig. 12(b). It might also be noted that growth shapes of metallic nanocrystals during deposition can differ from equilibrium shapes to amplify such distortion either in two dimensions[52] or three dimensions[53] by enhancing the prominence of a subset of step edges or facets. These observations suggest that 24% of triangular islands correspond to fcc Fe. Finally, we note that as for hcp structures, our continuum analysis assumes large linear cluster sizes of many lattice constants. For smaller nanoscale clusters, minority facets in the continuum formalism may not appear, and there will be some deviation in predictions of relative dimensions due to the discrete atomistic structure.[28]

F. Effect of T_{dep} on encapsulated clusters

The deposition temperature controls whether or not encapsulated clusters form, as presented in Sec. III A. This parameter also affects the amount of Fe on the surface, as shown in Fig. 13. At a fixed deposition time and with increasing temperature from 800 to 900 K, the amount of Fe adsorbed decreases steadily as reflected by the Fe/C XPS ratio in Fig. 13(a). This can be explained by a decreasing condensation coefficient[52,54] of Fe on graphite. Focusing only on encapsulated Fe clusters, the island density [Fig. 13(b)] shows a downward trend in parallel with a decrease in total Fe content, though the temperature range is much narrower for the density data than for the XPS data. The island dimensions exhibit weak variations that are not statistically significant in view of the large error bars shown in Figs. 13(c) and 13(d). Hence, the number density of encapsulated Fe clusters falls but their size remains roughly constant, as T_{dep} increases from 875 to 900 K. (The constant island size is somewhat accidental, just reflecting the feature that the amount of Fe on the surface decreases to the same degree as the density of Fe islands with increasing T_{dep}.)

G. Effect of deposition time on encapsulated islands: Evidence of coarsening

We also explore the effect of deposition time at fixed $T_{dep} = 900$ K. The XPS data in Fig. 14(a) show that the relative intensity of the Fe 2*p* peak increases nonlinearly with deposition time, approaching a plateau beyond 90 min. The island density [Fig. 14(b)] shows a maximum at 45 min. Meanwhile, the average island height and width increase with deposition time, though the uncertainties are again large [Figs. 14(c) and 14(d)].

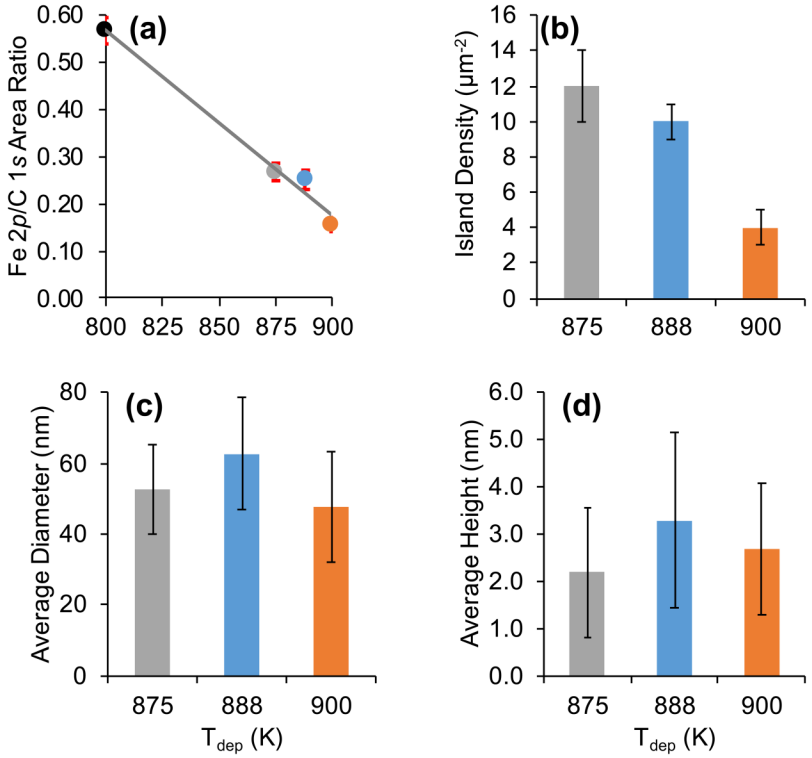

FIG. 13. (a) XPS determination of the relative amount of Fe on the graphite surface and (b)–(d) average characteristics of encapsulated Fe islands as functions of T_{dep}. The line in (a) is drawn to guide the eye. All at fixed deposition time of 90 min. In (c), the diameter represents the width of the flat island top.

These data may be interpreted as follows. At low deposition time, up to 45 min, the primary process is nucleation of new Fe islands. This leads to an increase in island density. Beyond 45 min, islands have sufficient time to coarsen significantly during deposition. This contributes to their increasing size and decreasing density. In fact, it is not uncommon to find islands that appear to have collided, leading to the interesting possibility that the ripening mechanism may be diffusion and merging of intact islands (Smoluchowski ripening).[55] Examples are evident in Figs. 2(a), 2(c), and 14(b) at 90 min. Further examples are shown in the supplementary material.[67] We note that the density of islands is so low that random growth-induced coalescence seems highly unlikely.

Another part of the interpretation is that, as islands grow taller, the XPS Fe signal is increasingly attenuated within the islands, explaining the nonlinearity in Fig. 14(a). This is made plausible by the observation that Fe $2p_{3/2}$ photoelectrons have a kinetic energy of 546 eV in these experiments, which corresponds to an inelastic mean free path (IMFP) of 1.08 nm in Fe (or 1.15 nm in graphite).[56] This IMFP is comparable to the average island height after 22.5 or 45 min of deposition, so minimal attenuation is expected after these short depositions. However, the IMFP is significantly smaller than the island height after 90 or 180 min, indicating attenuation after longer depositions.

H. Air-stability of encapsulated Fe

Fe oxidizes easily in ambient conditions. In order to test the stability of encapsulated Fe, we conducted oxidation experiments on two different Fe/graphite samples made at 875 and 900 K. Each sample was taken outside the UHV chamber and exposed to ambient conditions for 30 min. It was reintroduced to UHV where XPS was conducted. The sample was then subjected to the routine graphite sample outgassing procedure, i.e., it was heated at 800 K for 20 min. STM images of the outgassed samples were acquired, followed by additional XPS acquisitions.

We focus on the most prominent region, Fe $2p_{3/2}$, for the two Fe/graphite samples as shown in Fig. 15. (XPS spectra for the entire Fe 2*p* region are shown in the supplementary material.[67]) The black vertical line indicates the binding energy of the Fe $2p_{3/2}$ peak at 706.92 ± 0.05 eV for 875 K in Fig. 15(a) and 706.93 ± 0.06 eV for 900 K in Fig. 15(b), respectively. The values are consistent with literature values for bulk and nanoparticles of metallic Fe^0.[57–60] For both samples, the Fe $2p_{3/2}$ region becomes heavily distorted after air exposure, substantially suppressing the intensity of the Fe^0 peak. Two additional peaks can be assigned upon peak deconvolution. The peak that is outlined by short dashed lines at 709.40 ± 0.05 eV for 875 K and 709.42 ± 0.07 eV for 900 K indicates Fe^{2+} species, while the peak outlined by long dashed lines at 711.40 ± 0.05 eV for 875 K and 711.42 ± 0.07 eV for 900 K represents Fe^{3+} species, both in agreement with literature values.[57,58] Based on peak areas, the ratio of oxidized Fe to metallic Fe after deposition at 900 K and air exposure is 4:1.

Moreover, the O 1*s* region of the air-exposed sample (for instance, the sample made at 875 K) can be deconvoluted into three components, as shown in Fig. 14(c).

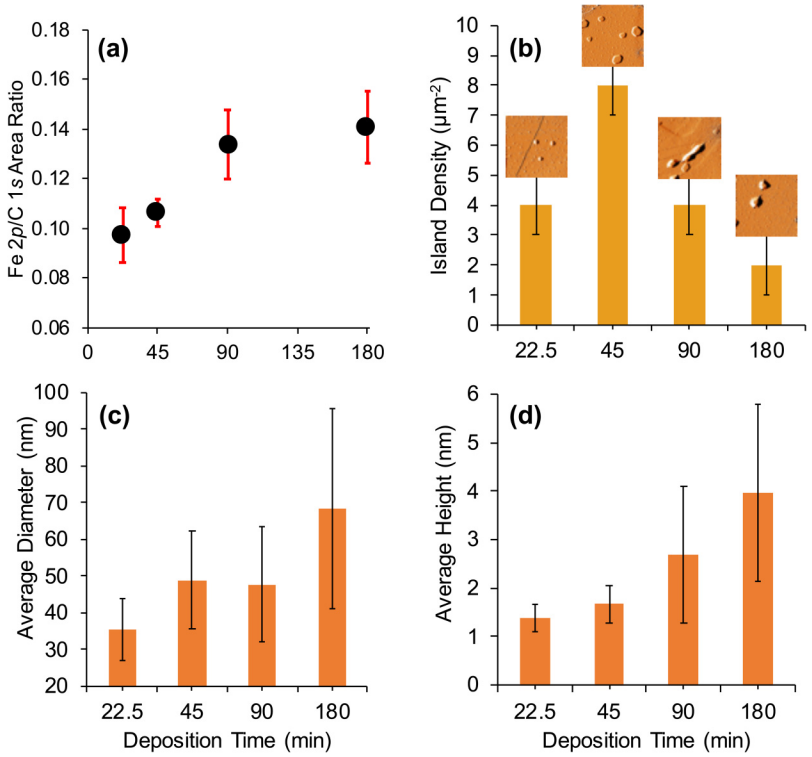

FIG. 14. Four separate Fe depositions at 900 K as a function of time, and the resulting (a) relative XPS peak intensity; (b) island density with insets of STM images corresponding to the island density; (c) average diameter of the flat island top; and (d) average island height. In (b), the STM image insets are $500 \times 500\,\text{nm}^2$. Tunneling conditions (tip bias) for STM insets, with increasing deposition time, are +2.0 V, 0.26 nA; +3.4 V, 0.26 nA; +2.8 V, 0.26 nA; and +2.5 V, 0.26 nA.

The peaks fitted at 530.34, 531.74, and 533.89 eV are consistent with O^{2-}, OH^{-}, and H_2O, respectively,[57] the former two being the majority species. These two exist in a ratio of 1.4:1 (oxide:hydroxide) based on XPS peak areas.

The most stable oxides and hydroxides of Fe are Fe_3O_4 and $Fe(OH)_3$,[61,62] respectively, which makes them plausible candidates after air exposure. A 2:1 mixture of Fe_3O_4: $Fe(OH)_3$ would nicely explain the relative XPS peak intensities (the O 1*s* ratio and the Fe $2p_{3/2}$ ratio). However, it is entirely possible that other Fe-O species are present and that the situation is more complex.[63,57]

A major question is, which Fe species oxidize during air exposure? There are three candidates: large bare Fe clusters, which are present on terraces after growth at 875 K but not at 900 K [Sec. III A and Fig. 1(c)]; small bare Fe clusters at defects (like those shown in Fig. 6); and encapsulated Fe

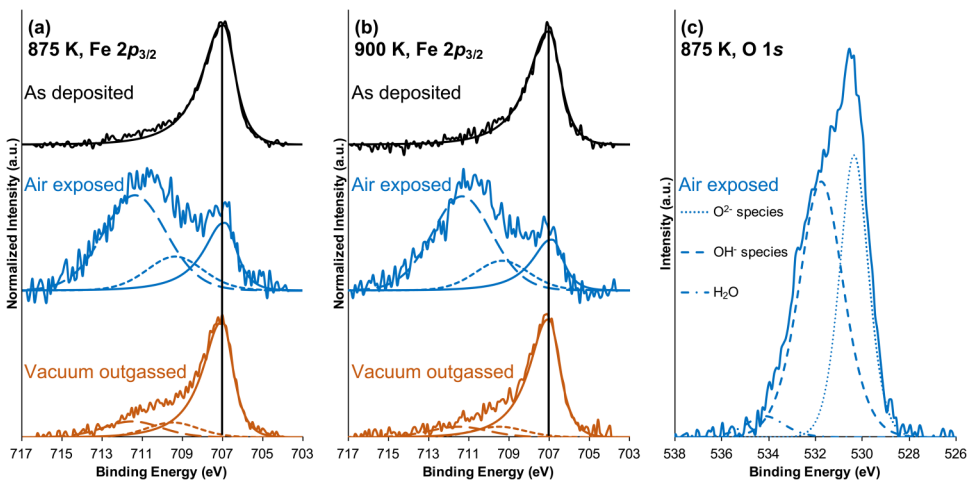

FIG. 15. XP spectra of the Fe $2p_{3/2}$ region of two separate Fe/graphite samples at different stages of sample preparation for the air exposure experiments. Time of deposition in both experiments is 90 min. In (a) and (b), the short dashed lines indicate Fe^{2+} species, while the long dashed lines show Fe^{3+} species. In (a) and (b), the XP spectra at each stage are normalized to the highest intensity at that stage.

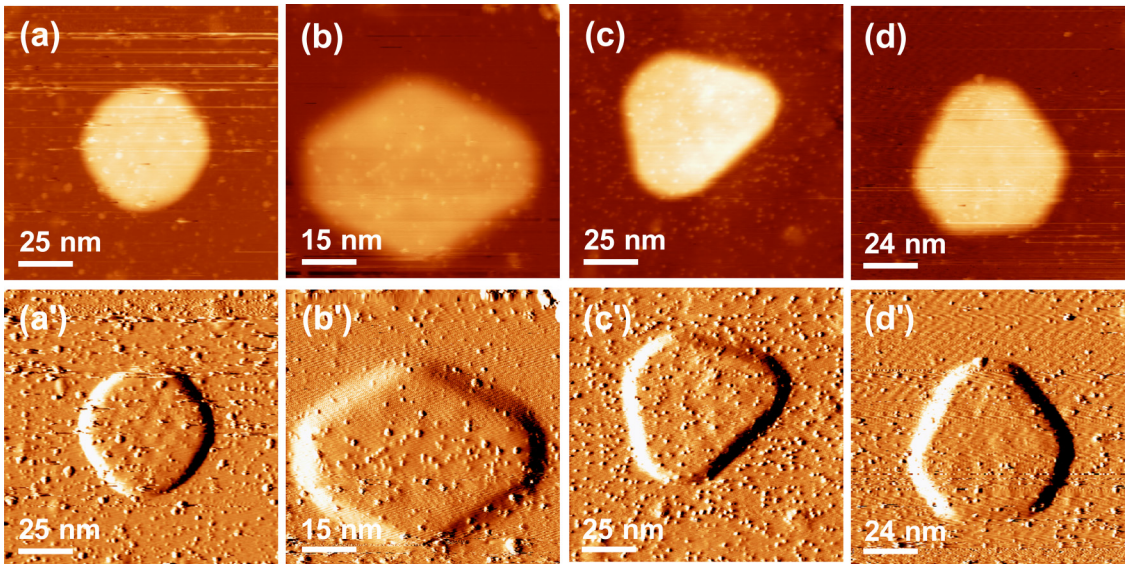

FIG. 16. STM images of encapsulated Fe clusters formed at (a)–(c) 875 K and (d) 900 K after air exposure and vacuum outgassing. Tip bias and tunneling current are (a) +3.8 V, 0.26 nA; (b) +1.8 V, 0.26 nA; (c) +1.7 V, 0.26 nA; and (d) +2.1 V, 0.26 nA.

clusters. We believe the answer is primarily the small bare Fe clusters at defects for the following reasons.

First, encapsulated Fe clusters can be imaged in STM, as shown in Fig. 16, after air exposure and vacuum outgassing. They are indistinguishable from encapsulated clusters that form immediately after deposition. It is possible that these islands oxidize under air exposure, then reform during outgassing without a trace of their oxidation, but this seems unlikely. More likely is that they remain protected and intact during air exposure.

Second, from Sec. III A, it is known that a few large bare Fe clusters exist on the terraces after growth at 875 K and even fewer at 900 K. Hence, the major spectral changes following air exposure must be due to either the small defect-anchored clusters or the encapsulated clusters. This is supported by the fact that there are only small differences between the XPS spectra of the air-exposed samples, for $T_{\mathrm{dep}} = 875$ K [Fig. 15(a)] and $T_{\mathrm{dep}} = 900$ K [Fig. 15(b)].

These observations lead to the following explanation. After Fe deposition, and after vacuum outgassing, the Fe $2p_{3/2}$ peak represents a combination of Fe in islands and small bare Fe clusters at defects. Air oxidation mainly affects the Fe atoms at the defects and leaves encapsulated clusters in the metallic state. Vacuum outgassing serves to deoxygenate the Fe atoms at defects, producing again a single peak in XPS. We also propose that the Fe atoms efficiently block the graphitic defects, so oxygen cannot penetrate the graphitic defects. This then serves to protect the encapsulated clusters.

IV. DFT RESULTS

A. Single Fe atom adsorption on, and intercalation in, graphite

When a metal cluster with n atoms is adsorbed on top of the graphite surface or intercalated underneath the top GML, the average interaction strength of one metal atom with its surrounding environment (including other metal atoms and substrate atoms) can be characterized by the chemical potential (at $T = 0$ K)

$$\mu_{\mathrm{M}} = \frac{E_{\mathrm{tot}} - E_{\mathrm{graphite}}}{n} - E_{\mathrm{M}}, \tag{1}$$

where M stands for a metal (M = Fe in this work), E_{tot} is the total energy of the metal-plus-graphite system, E_{graphite} is the energy of graphite substrate, and E_{M} is the energy of one metal atom in gas phase. For one adatom ($n = 1$) adsorbed on the substrate, Eq. (1) reduces to the conventional adsorption energy expression $E_{\mathrm{ads}} = E_{\mathrm{tot}} - E_{\mathrm{graphite}} - E_{\mathrm{M}}$. In the calculations of this section for one-metal-atom-plus-graphite systems, we always use a 4-ML graphite slab as the substrate, and the lateral size of the supercell is taken to be 6×6 in units of a_{C} (bulk graphite lattice, 0.2465 nm). During relaxation for energy minimization, the bottommost GML of the substrate is always fixed. The $\boldsymbol{k}$ mesh is taken to be $7 \times 7 \times 1$, and the energy cutoff is 600 eV. All these parameters have been carefully tested for energy convergence.

First, we examine the adsorption energies of one Fe adatom on top of the graphite surface after relaxation from the seven initial positions: TH, TT, HT, BM, MB, MM, and CC, defined in Fig. 17. The most favorable adsorption site is at HT with the lowest adsorption energy being −0.943 eV. The adsorption energies at TT and TH are −0.610, and −0.600 eV, respectively. The adsorption of the Fe atom at any site BM, MB, CC, or MM is unstable, and the adatom will move to a local minimum close to the initial site after full relaxation. Thus, the minimum energy path for diffusion of the adatom will be along HT to MB to TT. The lower limit of the diffusion barrier is about 0.33 eV. [For exact diffusion barrier, a climbing nudged elastic band (CNEB) calculation would be needed.]

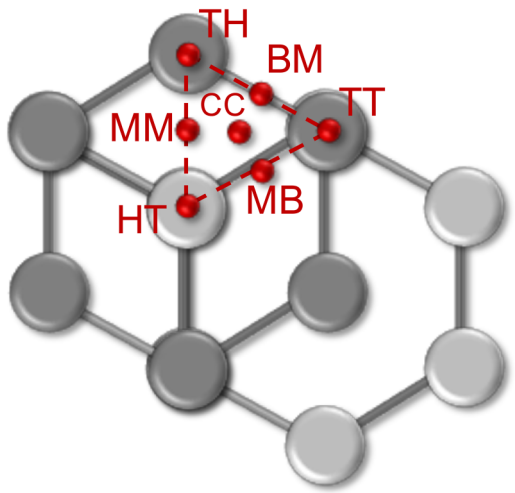

FIG. 17. Top view of seven initial positions (TH, TT, HT, BM, MB, MM, and CC) of a metal atom (red) with the graphite substrate for DFT calculations. Dark gray circles represent C atoms in the top (surface) GML, and light gray circles represent C atoms in the next layer below. The letters T, H, B, M, and C stand for top, hollow, bridge, midpoint, and center, respectively. The first letter denotes the location of the Fe atom with respect to the top (surface) GML, and the second letter denotes its location with respect to the second GML.

Next, we assess the energies of one Fe atom intercalated underneath the top GML. We find that any i site is more favorable than any t site (see Table II). The most favorable site is at iHT where $\mu_{Fe} = -2.414$ eV, which is 1.198 eV lower than the adsorption energy at tHT. (The iHT site is essentially degenerate with the iTH site.) Therefore, for one Fe atom, intercalation underneath the top GML is always more favorable than adsorption on top of the graphite surface. As an aside, we also note that both adsorbed and intercalated Fe atoms are magnetic (see Table II).

TABLE II. optB88-vdW results of chemical potential μ_{Fe} (in units of electron volts) and magnetic moment M (in units of bohr magneton per cell) for adsorption and intercalation of one Fe atom after full relaxation at different initial sites. The prefix "t" denotes adsorption on top of graphite, and the prefix "i" denotes intercalation beneath the top GML. Sites BM, CC, etc., are defined in Fig. 17 and its caption. μ_{Fe} is calculated from Eq. (1). $\Delta\mu_{Fe}$ is the energy relative to the lowest energy at site iHT.

Initial site	μ_{Fe}	$\Delta\mu_{Fe}$	M	Notes
tBM				Moves to tTT
tCC				Moves to tHT
tHT	−0.942	1.198	2.001	Local equilibrium
tMB				Moves to tHT
tMM				Moves to tHT
tTH	−0.600	1.541	4.149	Local equilibrium
tTT	−0.609	1.531	4.145	Local equilibrium
iBM				Moves to iTH
iCC				Moves to iHT
iHT	−2.141	0.000	2.004	Local equilibrium
iMB				Moves to iHT
iMM				moves to iHT
iTH	−2.140	0.001	1.982	Local equilibrium
iTT	−1.523	0.618	2.197	Local equilibrium

B. Fe complete layer adsorbed on and intercalated in graphite

We also calculate the energetics for a complete layer of Fe, i.e., a Fe film, supported on and intercalated in a graphite substrate. In these calculations, we choose a close-packed (hcp or fcc) over a bcc structure because the STM data show that the majority of islands are hcp or fcc. Furthermore, we choose hcp over fcc for two reasons: (1) the cohesive energy is larger (more favorable) for hcp than fcc from Table I and (2) an hcp Fe(0001) slab is nonmagnetic while an fcc Fe(111) slab is antiferromagnetic, making the hcp configuration more convenient for DFT calculations.

In these calculations, the Fe(0001) slab has variable thickness L and the graphite substrate, or graphene overlayer + graphite substrate, always has a total thickness of six GMLs. We always use a 1×1 supercell (in units of the optB88-vdW bulk graphite lattice constant $a_C = 0.2465$ nm). This implies an Fe-graphite lateral lattice mismatch of $(a_C - a_L)/a_L \times 100\%$, where a_L is the lateral equilibrium lattice constant of the Fe(0001) slab with thickness L. For a thick hcp Fe(0001) slab, $a_{L\to\infty} = a_{\varepsilon\text{-Fe}} = 0.2459$ nm from our optB88-vdW calculation, and then $(a_C - a_{L\to\infty})/a_{L\to\infty} \times 100\% \approx 0.244\%$, which corresponds to negligible tensile strain for the Fe film along the lateral direction. During relaxation for energy minimization, the bottommost GML of the substrate is always fixed. The $\boldsymbol{k}$ mesh is taken to be $51 \times 51 \times 1$, and the energy cutoff is 600 eV. In these calculations, we do not consider spin polarization because the most favorable structure of bulk hcp Fe(0001) is nonferromagnetic, as mentioned in Sec. II B.

We have carefully considered the effect of the symmetry of the lattice match between the Fe film and the graphite or graphene layer(s) and have performed numerous calculations spanning different symmetries. These are presented in the supplementary material.[67] In the discussion and comparisons below, for a given Fe film thickness L, we always take the most favorable configuration.

To analyze the interaction strength of an Fe film adsorbed on or intercalated in graphite, we calculate μ_{Fe} using Eq. (1), where the Fe cluster should be interpreted as a complete Fe(0001) film. In Fig. 18(a), we plot μ_{Fe} as a function of Fe film thickness L for Fe films adsorbed on and intercalated in graphite as well as freestanding Fe(0001) films. (The corresponding data for μ_{Fe} are listed in Table S5 in the supplementary material.[67]) The lower μ_{Fe} value indicates the stronger average interaction of one Fe atom with its surrounding. From Fig. 18(a), the Fe in the adsorbed film always has slightly stronger interaction than a freestanding film for any L, while an intercalated film always has significantly stronger interaction than an adsorbed film. When $L \to \infty$, these μ_{Fe} values tend to the negative of the cohesive energy (Table I) of bulk hcp Fe, as indicated by a dashed red horizontal line.

To illustrate more clearly that intercalation is more favorable for a given L, we plot ΔE_L in Fig. 18(b), where ΔE_L is the energy change per unit cell from adsorption to intercalation of the Fe(0001) film. From Fig. 18(b), for all L, $\Delta E_L < 0$, indicating that intercalation is always favored over

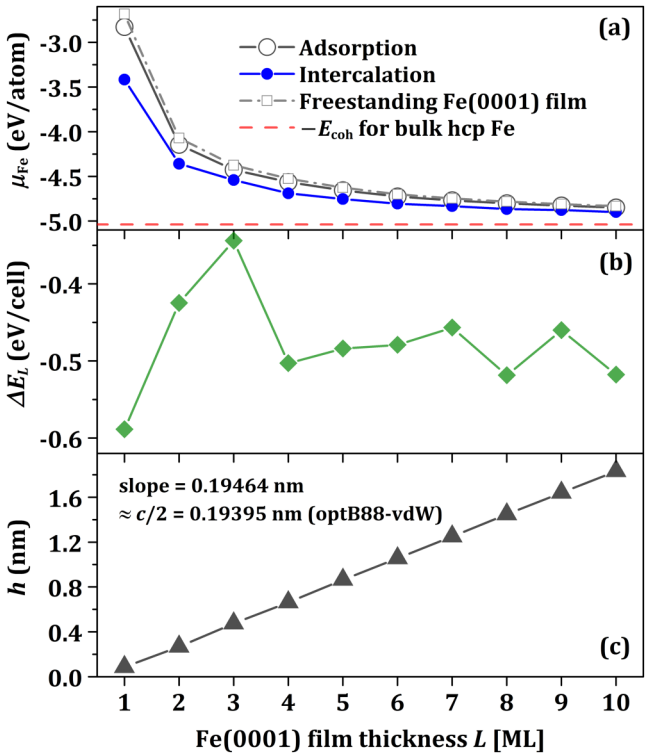

FIG. 18. (a) DFT curves of μ_{Fe} vs Fe(0001) film thickness L for adsorbed and intercalated Fe(0001) films. Dashed red horizontal line indicates the negative cohesive energy of bulk hcp Fe. (b) DFT energy difference ΔE_L per unit cell from adsorption to intercalation of an Fe(0001) film as a function of L. (c) The height h of top GML after intercalation of an Fe(0001) film with the thickness L, along the z direction perpendicular to the surface and measured relative to the top surface of the clean graphite slab before intercalation.

adsorption; for larger L, there are odd-even oscillations with increasing L. These oscillations are a result of the alternation of the upper metal-graphene interface structure between odd and even layers associated with the AB stacking of the hcp Fe film (given the fixed lower interface structure; see Sec. S4 in the supplementary material).[67] In addition, Fig. 18(c) shows that height h of the top GML is linear with a slope of 0.19464 nm, which is almost the same as the interlayer spacing $c/2 = 0.193\,95$ nm of hcp Fe(0001).

V. DISCUSSION

In this section, we will compare the observations for encapsulated Fe clusters with those reported previously for Cu, Ru, and Dy islands.[1–3] A summary of comparisons is given in Table III. Overall, we find that encapsulated Fe clusters bear a stronger resemblance to those of Cu than to those of Ru or Dy.

First, several features are common to encapsulation of all the metals. All require that the graphite surface be sputtered prior to metal deposition and that metal deposition be carried out with the graphite substrate at elevated temperature.[1–3] This points toward a common mechanism of encapsulation. We have proposed that this mechanism is diffusion of individual metal atoms through surface defects and into the subsurface carbon galleries, followed by nucleation, growth, and trapping within the galleries.[64] Elevated temperatures are necessary to prevent metal atoms from clogging the defects. In all cases, the density of encapsulated metal islands, N_{enc}, is only a small fraction of the defect density, N_{def}; for Fe, the ratio is $(1–6) \times 10^{-4}$. This leads to the conclusion that only a small fraction of defects serve as active portals by which metal atoms can access the subsurface galleries. We are currently working to determine the nature of those defects, although there are recent indications from the theory that a 2- or 3-atom vacancy allows passage of single metal atoms with a low activation barrier; a 1-atom vacancy is simply too small.[30,65]

Another commonality is that all three of the metals examined to date—Fe, Cu,[1] and Ru[2]—appear to be stable in air in their encapsulated form. For Ru, XPS shows no evidence of oxidation after air exposure alone, whereas both Cu and Fe show significant oxidation. We attribute the latter to the reaction of small bare metal clusters decorating defects, rather than oxidation of encapsulated clusters. In all three cases, both XPS and STM show that the original surface (after encapsulation) is recovered after vacuum annealing at 800 K, indicating that the encapsulated clusters are fully protected. We believe that the small bare metal clusters block the defects during air exposure, preventing permeation of oxygen and other gases.

Island dimensions and densities, however, serve to divide the four metals into two groups. On the one hand, there is Ru and Dy,[2,3] which have small islands and high island densities; the island heights are only a few atomic layers of metal, and diameters are on the order of 10–20 nm. On the other hand, there are Fe and Cu[1] with large islands and small island densities; their island heights are ten(s) of atomic layers of metal, and diameters are 50–76 nm on average. Because the islands of Fe and Cu are taller, there is often an obvious side slope that can even dominate the appearance of the island in STM. These shapes have been discussed elsewhere extensively for Cu, with some preliminary analysis of Fe;[39] a full detailed analysis of Fe is planned for future work.

Another feature which divides the metals is the number of graphene layers on top of the islands. For both Fe and Cu, evidence shows that there is more than one layer,[1] whereas for Ru there is only a single layer.[2,3] The evidence for Ru comes from the observation of a moiré pattern on top of the islands and the detailed appearance of the graphite lattice within the moiré.[40] The existence of multiple layers of graphene on top of Fe and Cu plausibly suppresses any possible moiré. At this point, it is unclear how the islands come to be buried beneath multiple graphene layers, but a driving force can be inferred from the observation (from DFT) that single adsorbed metal atoms always interact more strongly with graphite than with graphene.[54] This is also reflected in adhesion energies calculated for graphite or graphene interacting with Cu or Fe. For both metals, adhesion is slightly stronger with graphite than with a GML.[28,36] By extension, a metal island would be slightly more stable under a graphene blanket consisting of multiple graphene layers than under a single graphene layer.

TABLE III. Summary of key characteristics of encapsulated metal islands on graphite. For Cu, only multilayer islands (Ref. 1) are considered here. STM insets are all derivative images. Image size is $125 \times 125\ \text{nm}^2$ for Fe and Cu, and $35 \times 35\ \text{nm}^2$ for Ru and Dy. T_{dep} and tunneling conditions are Fe (900 K, +3.9 V, 0.27 nA); Cu (800 K, +4.6 V, 0.24 nA); Ru (1180 K, +1.0 V, 0.36 nA); and Dy (850 K, +1.5 V, 0.25 nA).

Metal	Maximum N_{enc} (μm^{-2})	Ratio of $N_{\text{enc}}/N_{\text{def}}$	Average (range) of heights, in metal atomic layers	Average (range) of widths of flat tops (nm)	No. of top graphene layers	Typical appearance in STM	Reference
Fe	12	$(1–6) \times 10^{-4}$	13 (6–60)	50 (17–140)	>1	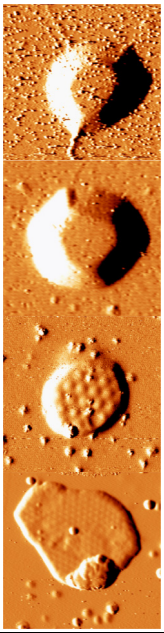	This work
Cu	55	$(4–8) \times 10^{-3}$	35 (10–200)	76 (30–570)	>1		1
Ru	600	5×10^{-2}	3 (2–4)	13 (8–18)	1		2
Dy	230	1×10^{-2}	3	16 (7–34)	?		3

Yet another factor to consider is the thermodynamic driving force for encapsulation. We have carried out DFT for all four metals, testing whether a film or slab of the metal is energetically favored in encapsulated or adsorbed forms. We find that the encapsulated slab is favored for Fe, Ru,[2] and Dy[3] but not for Cu.[1] Given that the metals divide into (Fe, Cu) versus (Ru, Dy) groups as discussed above, this suggests that thermodynamics is not the sole determinant of behavior. In the case of Cu, we have concluded that encapsulation occurs due to kinetics rather than thermodynamics: Single Cu atoms are more stable in the gallery than adsorbed on top of the surface, which favors a significant adatom population in the galleries.[1] When these adatoms nucleate into islands, they are trapped. Such kinetics may dominate for all metals, not just Cu, in which case the stability of a single atom is more relevant than the stability of a film. In this paper, we have shown that a single Fe atom is more stable in the gallery than in the adsorbed state, so the kinetic picture is certainly plausible for Fe as well as the thermodynamic one.

Finally, we return to the issue of reaction with carbon, introduced in Sec. I. The division of metals into (Fe, Cu) and (Ru, Dy) groups does not follow the lines expected if carbon solubility or carbide formation were important factors in cluster encapsulation. For instance, one might envision that the topmost graphene blanket would form by carbon dissolution in the metal at the deposition temperature, followed by precipitation upon cooling. This would be analogous to the established mechanism of graphene growth at the surface of bulk Fe, described in Sec. I. (This would, however, be at odds with the observation of a continuous graphene blanket joining the graphite substrate and the island top, as shown in Fig. 7(a″), for example. It would also be difficult to reconcile with wrinkling, attributed to delamination in Sec. III B.) In the precipitation-growth scenario for encapsulation, one would expect Fe to join the (Ru, Dy) group and the metal Cu to be much different. This expectation is not met. While it is indeed likely that carbon is dissolved in encapsulated islands of Fe, Ru, and Dy, it is unlikely that this plays a major role in the encapsulation process itself. Also, the absence of evidence of Fe carbide in XPS (Sec. III C) indicates that carbide does not play a role, analogous to our earlier conclusion for encapsulated Dy.[3,66]

In this paper, we have presented evidence that the encapsulated Fe clusters coarsen, perhaps, via Smoluchowski ripening (Sec. III F and supplementary material[67]). We propose that this occurs for Cu also[1] and that the major difference between the two groups of metals is whether or not this process occurs during growth. For Cu and Fe, ripening leads to a low density of large islands, whereas for Ru and Dy, lack of ripening leads to a high density of small islands. In the latter case, the observed configuration more nearly reflects the conditions of initial formation. This is a topic of continuing investigation in our group.

VI. CONCLUSIONS

In this paper, we have expanded the dataset of metals for which encapsulation is well-characterized at the surface of

graphite. We have accomplished this by adding Fe—a metal with a high affinity for carbon. By comparing it with other metals Cu,[1] Ru,[2] and Dy,[3] we conclude that the affinity for carbon is not relevant to the mechanism of encapsulation.

Other results of interest include the fact that shapes (footprints) of islands are consistent with metallic Fe, predominantly in the hcp or fcc form, though larger islands tend toward bcc. The hexagonally close-packed planes of the hcp and fcc structures are stabilized by their excellent lattice match with the graphite substrate. Evolution of island density with deposition time provides evidence of coarsening, perhaps via Smoluchowski ripening. The encapsulated islands are stable in air at room temperature, protected by small Fe clusters that decorate defect sites and block permeation of gases. DFT shows that two configurations of Fe are both more stable within the gallery than adsorbed on top of the surface: a single atom of Fe and a film (slab) of metallic Fe.

The experimental work was performed or supervised by A.L.R., D.J., M.C.T., and P.A.T. Theoretical work was performed or supervised by Y.H., K.C.L., and J.W.E.

ACKNOWLEDGMENTS

This work was supported mainly by the U.S. Department of Energy (DOE), Office of Science, Basic Energy Sciences, Materials Sciences and Engineering Division. The research was performed at the Ames Laboratory, which is operated by Iowa State University under Contract No. DE-AC02-07CH11358. The experimental work was performed or supervised by A.L.R., D.J., M.C.T., and P.A.T. Theoretical work was performed or supervised by Y.H., K.C.L., and J.W.E. Participation by K.C.L. and J.W.E. in the theoretical work was supported by the DOE, Office of Science, Basic Energy Sciences, Chemical Sciences, Geosciences, and Biosciences Division. DFT calculations were performed, in part, with a grant of computer time at the National Energy Research Scientific Computing Centre (NERSC). NERSC is a DOE Office of Science User Facility supported by the Office of Science of the U.S. DOE under Contract No. DE-AC02-05CH11231. The calculations also used the Extreme Science and Engineering Discovery Environment (XSEDE), which is supported by the National Science Foundation (NSF) under Grant No. ACI-1548562.

[1]A. Lii-Rosales, Y. Han, J. W. Evans, D. Jing, Y. Zhou, M. C. Tringides, M. Kim, C.-Z. Wang, and P. A. Thiel, J. Phys. Chem. C **122**, 4454 (2018).
[2]A. Lii-Rosales *et al.*, Nanotechnology **29**, 505601 (2018).
[3]Y. Zhou, A. Lii-Rosales, M. Kim, M. Wallingford, D. Jing, M. C. Tringides, C.-Z. Wang, and P. A. Thiel, Carbon **127**, 305 (2018).
[4]H. Okamoto, J. Phase Equilib. **13**, 543 (1992).
[5]G. A. López and E. J. Mittemeijer, Scr. Mater. **51**, 1 (2004).
[6]G.-Y. Adachi, N. Imanaka, and F. Zhang, "Rare earth carbides," in *Handbook on the Physics and Chemistry of Rare Earths* (Elsevier, New York, 1991), Vol. 15, Chap. 99, p. 61.
[7]N. R. Sanjay Kumar, N. V. Chandra Shekar, S. Chandra, J. Basu, R. Divakar, and P. C. Sahu, J. Phys. Condens. Matter **24**, 362202 (2012).
[8]Z. Zhao *et al.*, Nanoscale **6**, 10370 (2014).
[9]C. P. Kempter and M. R. Nadler, J. Chem. Phys. **33**, 1580 (1960).
[10]X. Chen *et al.*, Chem. Sci. **6**, 3262 (2015).
[11]N. A. Vinogradov *et al.*, Phys. Rev. Lett. **109**, 026101 (2012).
[12]Y. You, M. Yoshimura, S. Cholake, G.-H. Lee, V. Sahajwalla, and R. Joshi, Adv. Mater. Interface **5**, 1800599 (2018).
[13]X. Li *et al.*, Science **324**, 1312 (2009).
[14]X. Li, W. Cai, L. Colombo, and R. S. Ruoff, Nano Lett. **9**, 4268 (2009).
[15]J. M. Wofford, S. Nie, K. F. McCarty, N. C. Bartelt, and O. D. Dubon, Nano Lett. **10**, 4890 (2010).
[16]C. Mattevi, H. Kim, and M. Chhowalla, J. Mater. Chem. **21**, 3324 (2011).
[17]R. Muñoz and C. Gómez-Aleixandre, Chem. Vap. Deposition **19**, 297 (2013).
[18]T. Wu *et al.*, Nat. Mater. **15**, 43 (2015).
[19]P.-J. Hsu, J. Kügel, J. Kemmer, F. Parisen Toldin, T. Mauerer, M. Vogt, F. Assaad, and M. Bode, Nat. Commun. **7**, 10949 (2016).
[20]G. A. Somorjai and Y. Li, *Introduction to Surface Chemistry and Catalysis*, 2nd ed. (John Wiley & Sons Place, Hoboken, NJ, 2010).
[21]K. W. Kolasinski, *Surface Science: Foundations of Catalysis and Nanoscience* (Wiley, Chichester, 2008).
[22]W.-X. Zhang, J. Nanopart. Res. **5**, 323 (2003).
[23]J. R. Hahn and H. Kang, Phys. Rev. B **60**, 6007 (1999).
[24]H. A. Mizes and J. S. Foster, Science **244**, 559 (1989).
[25]G. Kresse and J. Furthmüller, Phys. Rev. B **54**, 11169 (1996).
[26]G. Kresse and D. Joubert, Phys. Rev. B **59**, 1758 (1999).
[27]K. Jiří, R. B. David, and M. Angelos, J. Phys. Condens. Matter **22**, 022201 (2010).
[28]Y. Han, K. C. Lai, A. Lii-Rosales, M. C. Tringides, J. W. Evans, and P. A. Thiel, Surf. Sci. **685**, 48 (2019).
[29]D. Bernal John and L. Bragg William, Proc. R. Soc. A **106**, 749 (1924).
[30]Y. Han, A. Lii-Rosales, M. C. Tringides, J. W. Evans, and P. A. Thiel, Phys. Rev. B **99**, 115415 (2019).
[31]H. C. Herper, E. Hoffmann, and P. Entel, Phys. Rev. B **60**, 3839 (1999).
[32]E. R. Jette and F. Foote, J. Chem. Phys. **3**, 605 (1935).
[33]C. Kittel, *Introduction to Solid State Physics*, 7th ed. (Wiley, New York, 1996).
[34]S. V. Radcliffe and M. Schatz, Acta Mater. **10**, 201 (1962).
[35]H. K. Mao, W. A. Bassett, and T. Takahashi, J. Appl. Phys. **38**, 272 (1967).
[36]A. Lii-Rosales *et al.*, "Shapes of Fe nanocrystals encapsulated at the graphite surface" (unpublished).
[37]M. M. Ugeda, I. Brihuega, F. Guinea, and J. M. Gómez-Rodríguez, Phys. Rev. Lett. **104**, 096804 (2010).
[38]F. Atamny, O. Spillecke, and R. Schlogl, Phys. Chem. Chem. Phys. **1**, 4113 (1999).
[39]S. E. Julien, A. Lii-Rosales, K.-T. Wan, Y. Han, M. C. Tringides, J. W. Evans, and P. A. Thiel, Nanoscale **11**, 6445 (2019).
[40]E. Sutter, D. P. Acharya, J. T. Sadowski, and P. Sutter, Appl. Phys. Lett. **94**, 133101 (2009).
[41]S. Marchini, S. Günther, and J. Wintterlin, Phys. Rev. B **76**, 075429 (2007).
[42]E. Hegenberger, N. L. Wu, and J. Phillips, J. Phys. Chem. **91**, 5067 (1987).
[43]D. D. L. Chung, J. Mater. Sci. **37**, 1475 (2002).
[44]G. Panzner and W. Diekmann, Surf. Sci. **160**, 253 (1985).
[45]F. Bonnet, F. Ropital, P. Lecour, D. Espinat, Y. Huiban, L. Gengembre, Y. Berthier, and P. Marcus, Surf. Interface Anal. **34**, 418 (2002).
[46]J. Shen, P. Ohresser, C. V. Mohan, M. Klaua, J. Barthel, and J. Kirschner, Phys. Rev. Lett. **80**, 1980 (1998).
[47]P. Ohresser, J. Shen, J. Barthel, M. Zheng, C. V. Mohan, M. Klaua, and J. Kirschner, Phys. Rev. B **59**, 3696 (1999).
[48]J. Shen, J. P. Pierce, E. W. Plummer, and J. Kirschner, J. Phys. Condens. Matter **15**, R1 (2003).
[49]E. Bauer and J. H. van der Merwe, Phys. Rev. B **33**, 3657 (1986).
[50]R. Tran, Z. Xu, B. Radhakrishnan, D. Winston, W. Sun, K. A. Persson, and S. P. Ong, Sci. Data **3**, 160080 (2016).
[51]J. Yu, X. Lin, J. Wang, J. Chen, and W. Huang, Appl. Surf. Sci. **255**, 9032 (2009).
[52]J. A. Venables, *Introduction to Surface and Thin Film Processes* (Cambridge University, Cambridge, 2000).
[53]E. Kaldis, *Current Topics in Materials Science* (North Holland, Amsterdam, 1979), Vol. 3.
[54]D. Appy, H. Lei, C.-Z. Wang, M. C. Tringides, D.-J. Liu, J. W. Evans, and P. A. Thiel, Prog. Surf. Sci. **89**, 219 (2014).
[55]K. C. Lai, Y. Han, P. Spurgeon, W. Huang, P. A. Thiel, D.-J. Liu, and J. W. Evans, Chem. Rev. **119**, 6670 (2019).
[56]S. Tanuma, C. J. Powell, and D. R. Penn, Surf. Interface Anal. **43**, 689 (2011).

[57]G. Bhargava, I. Gouzman, C. M. Chun, T. A. Ramanarayanan, and S. L. Bernasek, Appl. Surf. Sci. **253**, 4322 (2007).
[58]S. Suzuki, Y. Ishikawa, M. Isshiki, and Y. Waseda, Mater. Trans. **38**, 1004 (1997).
[59]D. Wilson and M. A. Langell, Appl. Surf. Sci. **303**, 6 (2014).
[60]H. Tian *et al.*, Chem. Eng. J. **313**, 1051 (2017).
[61]D. D. Wagman, W. H. Evans, V. B. Parker, R. H. Schumm, I. Halow, S. M. Bailey, K. L. Churney, and R. L. Nuttall, J. Phys. Chem. Ref. Data **11**, 1 (1982).
[62]D. Talbot and J. Talbot, *Corrosion Science and Technology* (CRC, Boca Raton, 1998).
[63]T. Tanupabrungsun, D. Young, B. Brown, and S. Nešic, "Construction And Verification of Pourbaix Diagrams For CO_2 Corrosion of Mild Steel Valid Up to 250C," in *CORROSION 2012*, (NACE International, Salt Lake City, Utah, 2012) p. 16.
[64]Y. Han, A. Lii-Rosales, Y. Zhou, C. J. Wang, M. Kim, M. C. Tringides, C. Z. Wang, P. A. Thiel, and J. W. Evans, Phys. Rev. Mater. **1**, 053403 (2017).
[65]L. Yu, C. Du, and X. Liu, Mater. Res. Express **5**, 025022 (2018).
[66]A. Lii-Rosales, Y. Zhou, M. Wallingford, C.-Z. Wang, M. C. Tringides, and P. A. Thiel, Phys. Rev. Mater. **1**, 026002 (2017).
[67]See supplementary material at https://doi.org/10.1116/1.5124927 for additional experimental details, XPS spectra of Fe, examples of merged Fe islands, and details for DFT calculations.

Patricia A. Thiel is a Distinguished Professor of Chemistry, and of Materials Science and Engineering, at Iowa State University. She is also a Faculty Scientist in the Ames Laboratory. She is known for her research on the formation and evolution of nanostructures on surfaces, and surface properties and structures of quasicrystals. She earned her B.A. in Chemistry at Macalester College in 1975 and her Ph.D. in Chemistry at the California Institute of Technology in 1981. After postdoctoral work at the University of Munich as an Alexander von Humboldt Fellow, she joined the technical staff at Sandia National Laboratories, Livermore, then moved to Iowa State University in 1983, where she was recognized with awards from the Camille and Henry Dreyfus Foundation and the A. P. Sloan Foundation, and by an NSF Presidential Young Investigator Award, early in her career. She has since been accorded many other recognitions, notably election to the American Academy of Arts and Sciences (2019), the David J. Adler Lectureship Award from the American Physical Society (2010), the Arthur W. Adamson Award from the American Chemical Society (2010), and the Medard W. Welch Award of the AVS (2014). She has won numerous teaching awards at Iowa State University. She has authored or edited about 300 scientific publications. She has served on numerous boards and committees for major scientific organizations and has been a member of editorial advisory boards for 10 journals. She is currently Associate Editor of the *Journal of Chemical Physics*. Her past service to AVS includes the Board of Trustees, Executive Committee of the Surface Science Division, Program Chair of the National Symposium, and Chair of the International Interactions Committee. Currently, she is a member of the AVS Board of Directors.

Her advice to her 16-year-old self would be: "Don't be afraid to ask questions, even though occasionally someone will use them to make you look bad. Asking questions until you get clear answers is the surest, fastest path to understanding, and the benefits far outweigh the risks."

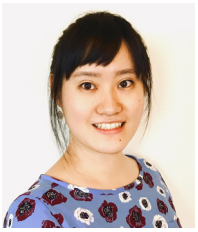

Ann Lii-Rosales is currently a postdoctoral research associate in Steven George's group in the University of Colorado Boulder. She earned her B.S. in Chemistry at Ohio State University in 2013 and her Ph.D. at Iowa State University in 2019 with the supervision of Patricia A. Thiel. Her Ph.D. project focused on the exploration of metal encapsulation beneath the *surface* of a layered material, graphite. The project resulted in the establishment of a synthetic strategy for metal encapsulation and discovery of novel surface nanostructures. Her graduate research work was recognized with the Nellie Yeoh Whetten Award from the AVS in 2018.